# Concept Validation for a Novel Stick-and-Slip, Light-Powered, Mobile Micro-Crawler

Jordan F. Klotz, Student, Member IEEE; Danming Wei, Student, Member IEEE; Zhong Yang, Student, Member IEEE; Ruoshi Zhang, Student, Member IEEE; Andriy Sherehiy; Mohammad N. Saadatzi, Member IEEE, Dan O. Popa, Senior Member, IEEE.

*Abstract* - **In this paper we present recent research results aimed at creating mobile micro-robotic agents powered by light energy. The SolarPede is a second-generation, cm-scale micro-crawler equipped with a legged locomotion system and an electronic backpack, targeting micro-factory applications. This novel micro-robot is an advancement in functionality and design over its decade-old predecessor, the ARRIpede, and includes technological advancements such as Bluetooth wireless communication, light power, and omnidirectional mobility on a flat substrate. The robot body consists of Micro Electro Mechanical System (MEMS) electrothermal actuators and micro-assembled vertical legs. Attached to the body is an electronic backpack realized using a custom-made Printed Circuit Board and interfaced to the body via a wire-bonded package. A simulation model for the SolarPede was created to predict system behavior and dynamic operation, and to serve as a design tool. Simulation results of leg motion were compared with experimental displacement measurements and the model was extended to the operation of the micro-robot in "belly-up" conveyor mode. Finally, optical microscopy was employed to experimentally measure the omni-directional motion of the SolarPede, and the robot power balance under a Solar simulator lamp was experimentally confirmed, thus validating the concept. Results suggest that continuous velocities of 15 µm/s can be achieved by the micro-robot in untethered operation.**

## I. Introduction

Future micro-factory applications require miniaturized mobile and fixed microrobots as envisioned by several research groups in recent work [1] [2]. Mobile micro-robots will be needed to reposition material in the micro-factory while being capable of wireless navigation and autonomous task execution. There have been many recent results in creating mobile microrobots for dry environments include cilia-like gated crawlers [3] [4] and light-powered PZT actuators [5]. Additionally, there are several well documented and tested positioning systems which utilize stick-and-slip effects [6] [7].

The ARRIpede [3] was an untethered, micro-assembled MEMS microrobot, capable of stick-and-slip operation while powered by an on-board Lithium-Polymer battery. While storing energy on-board for use during operation provides maximum operational flexibility, it is also technically challenging due to the unfavorable dimensional scaling of power sources. Therefore, it is desirable to harvest ambient energy, for instance from light sources, such that an onboard battery is not required.

The ARRIpede's gait and locomotion methods have been well characterized in past work and accompanied by stick-and-slip dynamical models [4]. This early design demonstrated a great payload carrying capacity in excess of 5g, and non-holonomic mobility characterized by forward only and large turn radii with speeds in excess of 1mm/s. However, the operation of this microrobot was seriously limited due to a short battery life (approximately 10 minutes), a nonholonomic motion dexterity on the substrate, and the lack of wireless communication for start, stop and feedback control.

In this paper we design and experimentally validate SolarPede, a new, solar-powered micro-crawler, sharing some design and fabrication traits with its ARRIpede predecessor, but overcoming many of its operational limitations. Microrobot actuation of the SolarPede is accomplished via electrothermal Chevron actuator banks and micro-assembled legs arranged in a differential drive configuration allowing omni-directional locomotion. A dynamic model was proposed to predict the system dynamic behavior and validated through experiments. Electronic backpack prototypes implementing Bluetooth wireless communication, solar-powered harvesting, and gait sequencing control were implemented and tested.

We report on results obtained to date validating that our concept is sound, including autonomous controlled operation of our micro-robot in "belly-up" conveyor mode. Results suggest that in the near future, a mobile SolarPede can be miniaturized to a cm-scale form factor for crawling operation required in micro-factory tasks.

The paper is organized as follows: in Section II we describe the SolarPede design and operational principles; section III discusses component selection, subsystem analysis, as well as models for dynamic simulation; in Section IV we present experimental results demonstrating concept feasibility; finally, Section V concludes the paper and discusses future work.

## II. Design, Fabrication and Operation

The SolarPede is envisioned as a legged crawler consisting of subsystems depicted in Fig. 1.

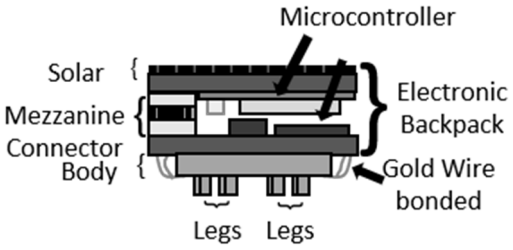


Figure 1. SolarPede Diagram with Component Layout.

The first subsystem is a MEMS device which serves as the body and holds the actuated legs of the micro-crawler. The second subsystem is the electronic "backpack" implemented as a pair of printed circuit boards, a solar panel and electronic components necessary for the robot's powered operation.

Authors are with the Next Generation Systems Group, Department of Electrical and Computer Engineering, University of Louisville, Kentucky, USA, email: jfklot01@louisville.edu.

978-1-7281-0948-0/19/$31.00 ©2019 IEEE

*A. MEMS Legs and Body*

The body of SolarPede is a cm$^2$ MEMS die with 8 chevron-type electrothermal actuators [8]. At the end of the shaft of the chevron actuators we included a so-called "Zyvex snap-fastener" [9] [10], into which a vertical, compliant MEMS leg is assembled perpendicular to the robot body. The electrical interconnects for these actuators are positioned on two edges of the die to make wire bonding the device into a die carrier easier to accomplish. The leg design is shown in Fig. 2, with dimensions chosen to accommodate the Zyvex socket, and to guarantee significant leg displacements of up to 50 µm. The "foot", that is the tip of the leg, was rounded to create a single point of contact between the leg and a substrate. This has the added benefit of mitigating errors in the event of a poor assembly resulting in a tilted leg.

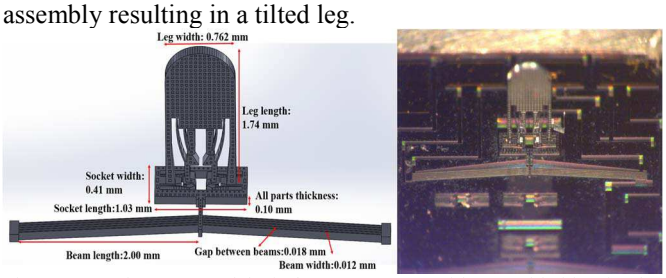


Figure 2. Left: CAD Model of Chevron actuator with assembled leg for the micro-crawler; Right: actual leg assembled for SolarPede.

Table 1. Design parameters for the assembled leg shown in Figure 2.

| ***Item*** | ***Measured Value*** | ***Item*** | ***Measured Value*** |
|---|---|---|---|
| Leg length | 1.74 mm | Beam length | 2 mm |
| Leg width | 0.762 mm | Beam width | 12 µm |
| Socket length | 1.03 mm | Beam gap | 18 µm |
| Socket width | 0.41 mm | Part thickness | 0.1 |
| Chevron angle | 3.4° | Beam number | 6 |

*1) Fabrication*

The body and legs of SolarPede are fabricated on a silicon-on-insulator (SOI) wafer with following parameters: the device layer is N-type with 0.01 to 0.02 Ω-cm resistivity, 100 µm thick device layer and <100> orientation; the buried oxide layer is 2µm thick and the handle layer is P-type with larger than 1000 Ω-cm resistivity and 500 µm thickness.

An RCA clean of the SOI wafer is performed as the first step of fabrication, to remove any organic, oxide and iconic contaminations, followed by photolithography to define the MEMS actuator features. A thin layer of chromium is then sputtered with a PVD-75 sputter under DC mode with 300W, to boost silicon-gold adhesion. A thick layer of gold for bonding points to the die package was sputtered under the same settings with longer sputtering time. Later, the metal is patterned with photolithography and then etched by gold etch and chromium etch consecutively.

Deep reactive ion etching (DRIE) was performed with a strong photoresist mask on the wafer. Etching time is derived from experience with the tool and checked under microscope to confirm finishing of etching. Before dicing the wafer, a protective layer of photoresist was spun to prevent debris from damaging or jamming the moving features. After dicing, selected dies were submerged in 49% hydro-fluoric acid to release moving parts from the wafer surface. Eventually, all released dies were dried by critical point dryer (CPD) to finish the fabrication process.

*2) Layout and Assembly*

Compared with ARRIpede microrobot shown in Fig. 3, which has only directional locomotion [3], new leg arrangements were configured to explore omnidirectional motions corresponding to the layout in Fig. 4, the SolarPede omnidirectional design. The inspiration of the placement of legs in these designs comes from similar mecanum wheels or differential drive arrangements for larger modern mobile robots. In this paper we study the omnidirectional design of Fig. 4 in detail.

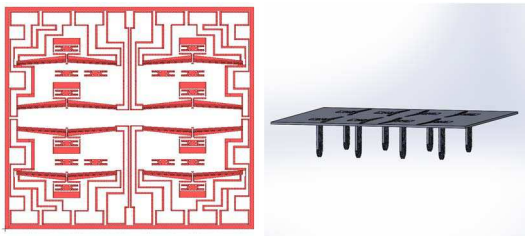

Figure 3. SolarPede L-Edit mask #1 (ARRIPede) and CAD model [3].

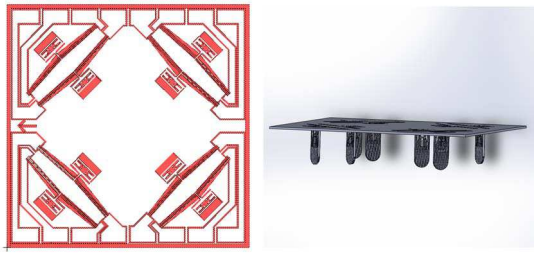

Figure 4. SolarPede L-Edit mask #2 (omidirectional) and CAD model.

To assemble the legs on the SolarPede base, a custom micro-assembly system, called NeXus, was employed. The NeXus includes two manipulators ($M_1$ holding a microgripper and $M_2$ holding the MEMS die substrate) and three imaging systems as shown in Fig. 5. $M_1$ consists of two motorized linear stages and one motorized rotation stage to realize X-Y-Θ three degrees of freedom (DOFs). $M_2$ consists of a XYZ motorized stage, a motorized rotation stage, and an extra manual XY stage to present 6 DOFs.

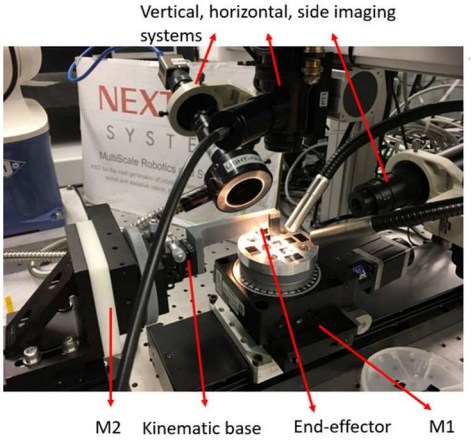


Figure 5. NeXus: a custom micrassembly system for SolarPede.

An end-effector mounted with micro-jammer is connected to manual XY stage by kinematic base. Fig. 5 also shows the three imaging systems that provide excellent views for the assembly processing from vertical, horizonal and side

direction. The legs were picked up and placed into sockets by micro-jammer, and then used UV sensitive epoxy to increase the mechanical strength between the connection.

*3. Principle of Operation*

The SolarPede micro-crawler achieves locomotion using stick-and-slip effects between the legs and the substrate, in a manner thoroughly discussed in [3], [4]. By timing the displacement of the legs, a forward gate motion can be obtained for which the velocity is proportional to the amplitude-frequency product of the leg. Unlike the nonholonomic design of the ARRIpede, the SolarPede contains actuator arrays which can be controlled to generate more dexterous maneuvers on the substrate. The holonomic motion methodology for SolarPede is presented in Fig. 6. For up-down and left-right four directional motion, only four legs are actuated to create motion. Otherwise for turning left or right, the legs are actuated by different frequency or applied voltage to generate different displacement of each side and produce turning motions.

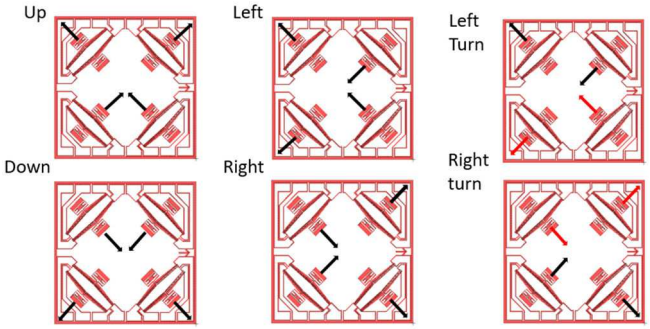


Figure 6. Theoretical vectors of holonomic motion methodology for SolarPede omnidirectional leg arrangement. Red vectors indicate motion performed at lower frequencies than black vectors.

## B. Electronic Backpack

Powering and control for the SolarPede is accomplished through an electronic backpack mounted onto the robot body. The backpack contains a power system and micro-controller, as depicted in the diagram Fig. 7. The power system is used to supply the MEMS actuators directly while the control system regulates which actuators are connected to the power systems at a given moment. These work in conjunction to create the gait patterns required for steerable motion.

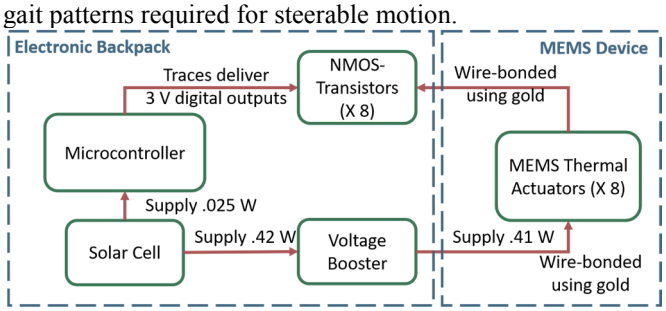


Figure 7. System diagram showing components with power requirements observed during experimentation.

*1) Voltage Booster*

To move the Chevron actuators on the microrobot, a minimum voltage of approximately +8V is required; however, to obtain sizable micron-scale displacements, voltages in excess of 20 V are needed. A voltage booster and supporting components are placed on one side of a printed circuit board, and converts +3.3 V applied at power source input which will produce an output in excess of +20 V. This target output value was chosen based on tests for the thermal chevron actuators used in our previous work with microrobots ARRIpede [4] and AFAM [11]. The SolarPede utilizes a TPS55340 Booster, Texas Instruments, USA due to its output characteristics and low power input requirements. The following equation from the voltage booster data sheet can then be used:

$$V_o = 1.229\left(\frac{R_1}{R_2} + 1\right) V_{in}, \quad (1)$$

in which $R_1$ and $R_2$ are tunable resistors. To fulfill system requirements, these values are chosen to be 160k and 10k respectively which results in an output voltage of 20.9 V from an input voltage of 3.3 V.

*2) Transistor Array*

The transistor array serves the purpose of regulating current to the Chevron actuators and stopping the flow of current to the legs when actuation is not desired. The drain of an N-Channel MOSFETs will be connected individually to the second pin of the thermal actuators. When an input of 1.8 V or greater is applied to the gate of the transistor, the circuit will be complete, and actuation occurs. The boosted voltage will be applied to one pin on of the 8 actuators in the MEMS system. Transistors will be placed in series with the actuators and be used to control which actuator is heated. The array itself will consist of 8 DMN62D0U (Diodes Inc., Plano, Texas, USA) transistors all of which will be mounted to the bottom of the electronic backpack, near the legs for easy access during wire-bonding. These were chosen to accommodate the 3.3 V output of the microcontroller as well as the drain voltage of 20.9 V.

*3) Micro Controller and Solar Cell*

A micro controller is mounted onto the electronic backpack to serve both the role of communicating with the user and controlling the gait patterns of the robot. The microcontroller is connected to the transistor array via traces and to the solar cell through a simple two wire connection. We selected an advanced, Bluetooth enabled microcontroller, the BL652 by Laird Corporation, Houston, Texas, USA, to serve in this role based on additional communication and power requirements discussed in Section III.

Among the primary concerns with the SolarPede designs is the goal of keeping the system completely untethered. To accomplish this, input power is provided directly to the voltage booster from a solar cell that allows the operation of the robot under an artificial white light source. The solar cell in our prototypes, is a 3 V Solar Cell, Solar Made Corporation, Colorado, USA, and was selected to balance the power consumption of the micro-actuator, with the power generated on a limited 20 mm x 20 mm footprint.

# III. Analysis and Simulation

## A. Leg Displacement and Stick and Slip Models

The SolarPede's motion is caused by overcoming the static friction under its feet as well as at the joints in the heating cycle, followed by the whole robot body movement in the cooling cycle. Fig. 8 depicts a lumped mass-spring-damper model of the robot's leg. In this model, $M_l$ and $M_b$ are the leg's

mass and the robot body mass, respectively, while K represents the stiffness and B is the damping coefficient of the Chevron actuator.

In this model, two friction forces combine to resist motion inputs from the Chevron actuator: one between the foot and substrate, $f_1$, and another at the joint between the leg and the robot body, $f_2$. Following Newton's second law of motion, the dynamic equations of this system can be written as:

$$M_l\ddot{X}_l = -F_a + f_1 + f_2 + K(X_b - X_l) + B(\dot{X}_b - \dot{X}_l) \quad (2)$$

$$M_b\ddot{X}_b = F_a - f_2 - K(X_b - X_l) - B(\dot{X}_b - \dot{X}_l) \quad (3)$$

$$f_1 = \mu(M_b + M_l)g \quad (4)$$

$$f_2 = \mu M_b g \quad (5)$$

where $\mu$ is the coulomb friction coefficient switching between static $\mu_s$ and dynamic $\mu_d$ in the stick and slip phases of leg motion, respectively, $F_a$ is the Chevron actuator electro-thermal force generated by an input voltage $V$, and $X_l$ and $X_b$ are the corresponding displacements of $M_l$ and $M_b$.

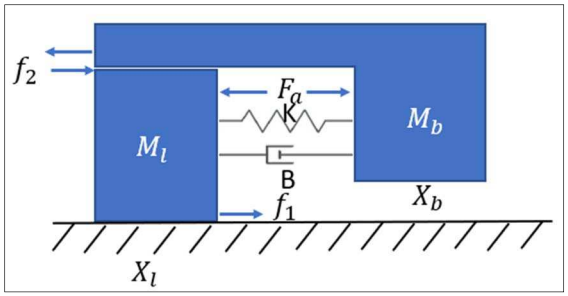


Figure 8. Mass-spring-damper model of the SolarPede's leg and body.

The value of $F_a$ during actuation cycles can be empirically estimated from steady-state displacement of the Chevron actuator according to a first order model:

$$F_a(V,f) = \frac{2NAEsin^2(\theta)}{L} \cdot \frac{\lambda V^2}{1+s\frac{f}{f_{BW}}} \quad , \quad (6)$$

in which $N$=6 is the number of Chevron beams, $E$ is the Young's modulus of $Si$, $\Theta$ is the bent beam angle, in our case 3.4°, $A$ is the cross-sectional area of the actuator, $V$ is the input voltage, $f$ is the actuator frequency, $f_{BW}$ is the actuator bandwidth, and $\lambda$ is an empirical constant.

Values for simulation of leg motion were selected according to the dimensional parameters of the actuator and leg, in particular $K$=185 N/m, $M_l$=0.3mg, $M_b$=0.25g, while $\lambda$ and $f_{BW}$ were estimated from experiments as 0.03 and 50 Hz, respectively (see section IV-B). Furthermore, assuming that the coefficients of friction for Silicon-Silicon contact were $\mu_s$=0.4, and $\mu_d$=0.33, we estimated the forward velocity of the leg-body model as shown in Fig. 9. Simulation results indicate that we should expect forward velocities greater than 10 µm/s for a wide range of frequencies if the actuator voltage is 20 V. Fig. 9 also suggests that velocities increase parabolically with an increase of the supplied actuator voltage but will decrease with the gait frequency.

*B. Communication*

An extensive study of micro robotic communication methods was conducted to ensure that SolarPede is equipped with the optimal system for its scale and application. The following communication methods were evaluated: Wi-fi, Infrared, ZigBee, Terahertz, Bluetooth (and BLE) 4.0/4.2, and Bluetooth (and BLE) 5.0. The technologies were evaluated based on reliability, scale, range, data transfer speeds, power consumption, and examples of success at a scale appropriate for SolarPede. Protocols were compared in each category and were assigned points based on their placement in each category (5 for 1st, 4 for 2nd, etc.), as summarized in Fig. 10.

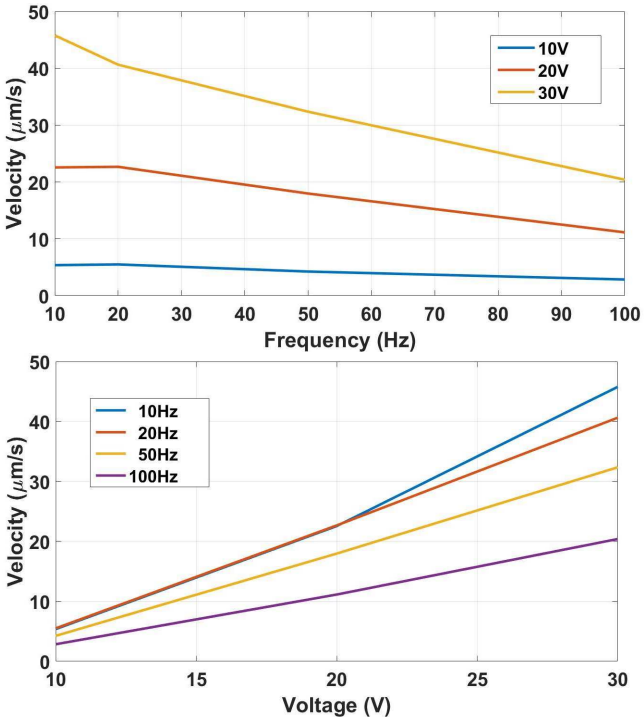


Figure 9. Plot of microrobot body velocity $X_b$ vs. leg actuation frequency (top) and voltage (bottom).

| | Range | Data Rate | Reliability | Size | Power Cons. | Existing Micro Robots | Total |
|---|---|---|---|---|---|---|---|
| *Wi-fi* | 4 | 5 | 5 | 1 | 1 | 3 | 19 |
| *Infrared* | 1 | 4 | 4 | 4 | 2 | 5 | 20 |
| *TeraHertz* | 2 | 3 | 1 | 5 | 5 | 1 | 17 |
| *Bluetooth 4.2* | 3 | 1 | 2 | 2 | 3 | 4 | 15 |
| *Bluetooth 5.0* | 5 | 2 | 3 | 3 | 4 | 2 | 19 |

Figure 10. A comparison of communication methods with columns denoting placement from 1st to 5th rank with methods receiving point values of 5 to 1 respectively. The final column shows total points accrued during comparison. Rows show individual ratings in the evaluated categories.

Infrared, Wi-fi, and Bluetooth 5.0 all received very similar performance marks, so a decision was made to weigh module size as the determining factor. With this decision, Wi-Fi was eliminated. With only two choices remaining, Bluetooth 5.0 was chosen because SolarPede is to be powered by laser or a similar white light source. It is likely that interference may occur if an infrared communication method is used while under this type of operation.

The selected Bluetooth 5.0 module (BL652) features 32 customizable I/O ports called Special Input/Outputs (SIO) which can be individually configured to digital in/out, analog in/out, PWM, or frequency modes (2 only for frequency mode). As manufactured, the BL652 contains a built-in antenna, and it occupies a surface area of 140 mm$^2$.

### C. Power Analysis

By experimentation, we measured that that the micro controller, even while broadcasting, requires only 24 mW of power. The voltage booster does not have strict input requirements for operation, but input power has a direct impact on power available at the output to the chevron actuators. Using experimental measurements of displacement vs input power (see Section IV-B), we estimated that a minimum of 0.3 W of power is required to generate at least 5 µm leg strokes, the minimum amount of individual leg displacement that SolarPede requires to move its payload. As a result, we concluded that 0.35 W is the minimum power that the solar cell must provide to the microrobot.

## IV. Experimental Results

Several experiments were performed to test electrical stability, validity of component selection, and overall performance of SolarPede prototypes. For ease of testing and programmability, the circuit was set up on a breadboard. The MEMS devices were wire bonded using gold wire into individual die carriers and placed directly into the breadboard and the array of transistors.

### A. Program and Signal Generation

The Laird BL652 module can be interfaced through Uart, SPI, I2C, VSP, and JTAG connections and is programmed using a custom language called *smart*BASIC. The program begins by broadcasting the BL652's address to a Bluetooth compatible phone or computer. Once connected using the Laird app or terminal, a virtual serial port is opened. The user can then transmit a string of characters to SolarPede. A simple case switch interprets the user input and performs a routine based on the user's selection. The routines SIO (set to digital outputs) to digital high or low in a pattern. The patterns are "forward", "left", "right", and "idle". The user can also select "complete" to stop the program and "testing" to activate only one leg. As a final feature, each time a user is prompted to select a gait option, he or she can also select a delay associated with the square wave. For the experiments, a voltage of +20 V is applied to the drain of transistors on the SolarPede circuit. The BL652 SIO are used to generate square waves with an amplitude of 0 or 3.3 V. These signals are tied to the gates of the transistors such that when the output is high, the transistor is closed, and current can pass to the corresponding microactuator.

### B. Leg Actuation and Circuit Validation

The "testing" feature of the program was used to generate a signal only to a select leg. This leg was positioned in line with a laser displacement sensor (LK-H008 sensor head with a LK-G5001 controller, Keyence Corporation, USA) which was used to measure the displacement of the leg during operation. Starting with 5V and increasing to 30 V, the displacement at these values were recorded. The input power was calculated based on the applied voltage and plotted against the displacement observed under the laser. Figure 11 presents the results and demonstrates a fairly linear relationship between power and displacement.

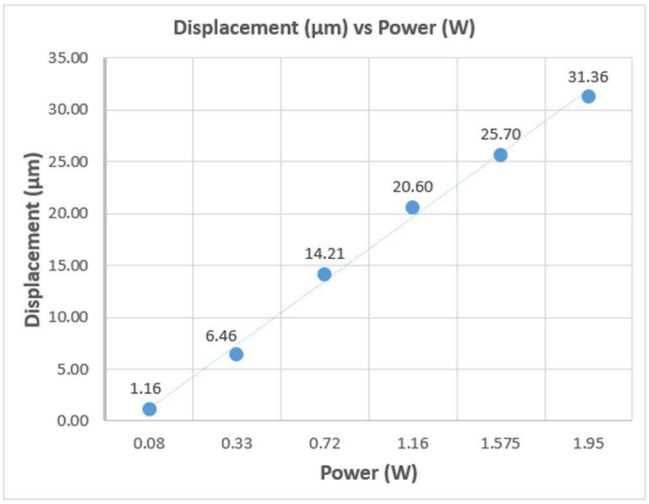


Figure 11. The blue line marks a comparison between displacement in µm on the Y axis and input power in W on the X axis.

Once the average displacement was measured in a steady environment, an experiment was performed to test the leg's behavior with varied voltage and frequencies. Leg displacement results from relevant combinations of voltages and frequencies can be seen in Table 2. Using the data collected, 60 samples were taken from the wave forms and used to calculate the mean and standard deviation of the displacement. The nominal operating range for the SolarPede was determined to be from 0 to 50 Hz. When larger frequencies, such as 200 Hz are applied, the actuators do not have enough time to cool. As a result, they will not retract from the steady-state displacement.

Table 2. Shows input voltage to the Solarpede leg, the frequency of 3.3 V amplitude square waves at the transistor gate, the typical maximum actuation in micrometers, and its standard deviation.

| *MEMS actuator Voltage* | *Gait Frequency* | *Average displacement* | *Standard Deviation* |
|---|---|---|---|
| 10V | 10 Hz | 2.96 µm | 0.01 µm |
| 10V | 20 Hz | 3.03 µm | 0.02 µm |
| 10V | 50 Hz | 2.34 µm | 0.07 µm |
| 10V | 100 Hz | 1.57 µm | 0.14 µm |
| 20V | 10 Hz | 12.42 µm | 0.04 µm |
| 20V | 20 Hz | 12.48 µm | 0.03 µm |
| 20V | 50 Hz | 9.89 µm | 0.21 µm |
| 20V | 100 Hz | 6.14 µm | 0.50 µm |
| 30V | 10 Hz | 25.20 µm | 0.07 µm |
| 30V | 20 Hz | 22.37 µm | 0.02 µm |
| 30V | 50 Hz | 17.81 µm | 0.34 µm |
| 30V | 100 Hz | 11.24 µm | 0.96 µm |

The results shown in Table 2 suggest that frequencies of 50 Hz may not be effective for actuation, because the leg does not reach a steady state in the short time that the voltage is applied. Due to the short switching time, the leg displacement is much smaller than at lower frequencies.

The program utilized in the single leg experiments was modified for a test with multiple legs while still in "belly up" mode. 30 V at 1 and 10 Hz were applied to actuate multiple legs. While 1 Hz is not very a practical frequency for the actual motion of the robot, it allowed the human eye to easily

perceive the leg's motion and helped to troubleshoot errors in the gait patterns. The assembled legs can be seen in Fig 12 A.

*C. Payload Experiments.*

To simulate the operation of the assembled SolarPede, the circuit used during program and component validation was wired to the die carrier. The SolarPede legs were breadboarded and connected to a power supply. The legs were placed in series with transistors which were connected to the SIO of the BL652. A payload cut from a silicon wafer was placed directly onto the legs of SolarPede, and the legs were actuated as described below to create motion of the payload. Placing a payload on the legs in this manner simulates the upright actuation of the robot under its own weight. The motion of this payload was recorded with a microscope camera and the resulting footage was used to determine speed.

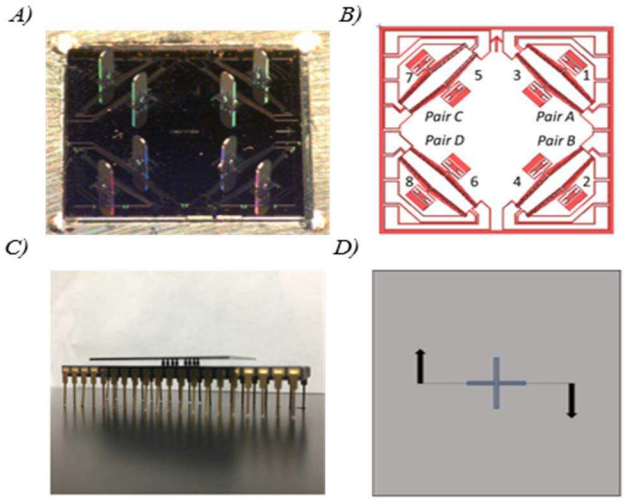


Figure 12. A: Assembled SolarPede Legs; B: Legs labled as in program with pairs marked; C: MEMS die wirebonded and in a package with payload resting on top; D: Vectors for payload motion under rotation gait sequence.

To protect the integrity of the equipment, light payloads were used initially. The die carrier was placed into the breadboard as before and the motion of 0.5, 0.6, and 1.2-gram payloads were recorded using a camera. The payload can be seen in Fig. 12 C. A scratch was made on the surface of the silicon payload to make tracking the payload easy to monitor and the result is shown in Fig. 12 D. The payloads were tested in succession having their motion recorded before switching to the next payload increasingly heavy.

During experimentation, we observed that when each leg was actuated individually, the payload was not moving. If, however, the actuators were paired and moved in a synchronized manner the payload experiences a larger actuation force, breaking static friction. The actuators were numbered and paired as shown in part A of Fig. 12. To achieve motion toward the left with respect to the ID mark individual legs were actuated in the sequence shown in part B of Fig, 13. There is a point where leg 3 is being disengaged and leg 1 is being engaged. The combined backward motion of leg 3 and forward motion of leg 1 creates double the net force of a single leg and is referred to as *Pair A* and marked in part B of Fig 12.

The gait sequence in Fig. 13 can be further summarized as *Pair A, Pair B, Pair C,* then *Pair D* in that order. By changing the order of the sequence, the pairs can be reversed. For example, actuating leg 1 then releasing it while engaging leg 3 results in a backward motion of *Pair A.* By reversing all 4 *Pairs,* motion opposite to the prescribed sequence occurs which results in motion away from the ID mark. By re-ordering the sequence and leg actuation, one can achieve motion in any of the cardinal directions similar to Fig. 6. The sequences shown in Table 3 show the input to displacement relationship observed during experimentation.

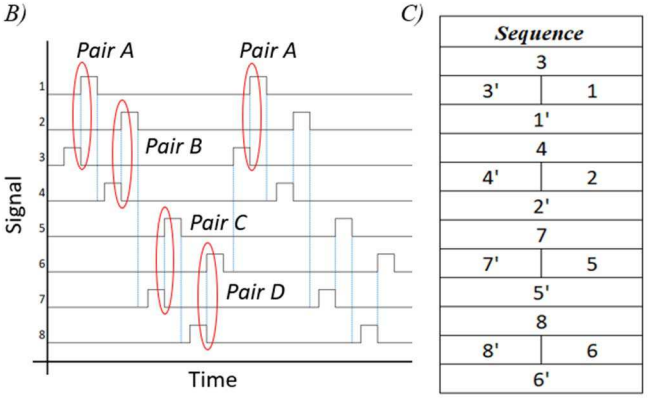


Figure 13. A: Output signals sent to legs with circles denoting syncronized actuation of two legs. B: Gait sequence with ' denoting digital low.

Table 3. Pair sequence where X indicates movement toward the outer edge of the substrate and X' indicates movement toward the interior of the substrate. A, B, C, and D correspond to Pairs shown in Fig 13. The direction of motion indicates payload travel with respect to the ID mark in Fig 13.

| *Paired Leg Actuation Sequence* | *Direction of motion* | *Observed Displacement (over 10 seconds)* | *Observed Velocity* |
|---|---|---|---|
| A-B'-C-D' | UP | 155 µm | **15.5 µm**/s |
| A'-B-C'-D | DOWN | 121 µm | 12.1 µm/s |
| A-B-C'-D' | LEFT | 133 µm | 13.3 µm/s |
| A'-B'-C-D | RIGHT | 113 µm | 11.3 µm/s |
| A'-B-C-D' | Rotate CW | - | 3 mrad/s |

SolarPede can also make its payload turn by setting half of the legs in reverse. By actuating any two pairs of legs that share an edge in the opposite direction of those on the other edge, rotation can be achieved as indicated in the results of Table 4, last row. Vectors of motion can be seen in Fig. 12 D.

*D. Solar Power Experiments*

An experimental set up was assembled for tests with solar cells used as a power source for our SolarPede. Directed at this power source was a solar simulator from Newport Corporation, Irvine, USA, including a Xenon arching lamp (Newport 67005) with its power supply and controller (Newport 69907). The solar cell used in our tests had a size of ~20 mm x ~ 24 mm and was able to supply 3.3 V and 20 mA under standard conditions (sunlight). Upon exposure to the solar simulator's light, we can achieve higher currents by focusing the light and increasing its intensity. The setup for this experiment can be seen in Fig. 14. We performed characterization of our solar cell, determining dependence of the supplied power by the cell on the power of the Xenon lamp. The light was applied to the input of the TPS55340 and the output from the booster was connect to the input of one of the Chevron actuators through a bread board. The recorded

relationship between the intensity of the light delivered and the displacement of the leg can be seen in Fig 15.

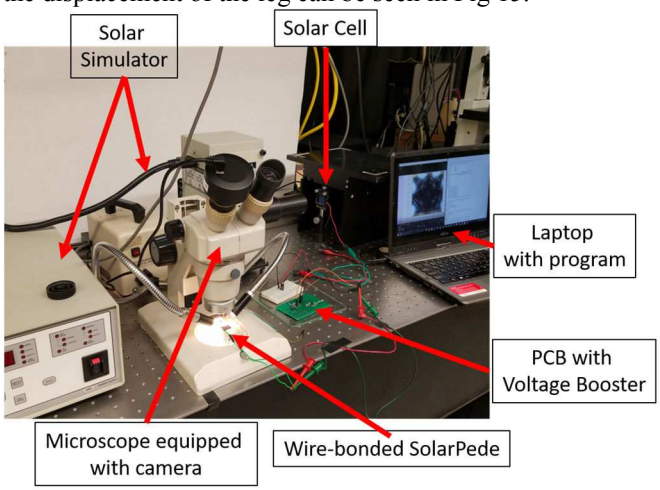


Figure 14. Solar Simulator with solar panel.

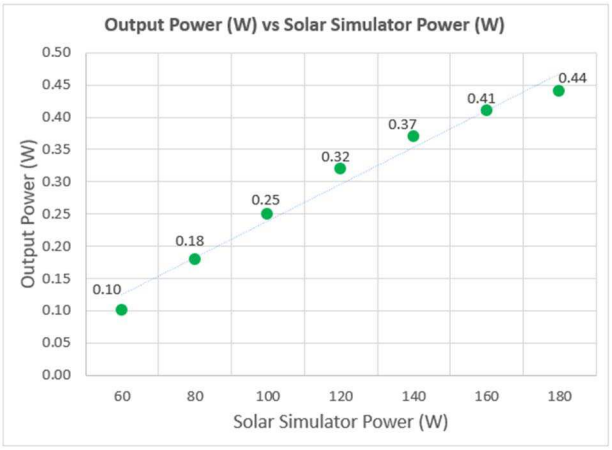


Figure 15. The X axis denotes the Solar Simulator input power and the Y axis denotes the output power from solar cell/input to the voltage booster.

Comparing the graph in Fig. 15 to the observed displacement vs input power of a single leg depicted in Fig. 8, we can conclude that at a range of 160 to 180 W light power on the solar simulator, the solar cell can generate microrobot power in excess of 0.33W. This produces a displacement between 6.46 µm and 14.21 µm for each microrobot leg.

## V. Conclusions and Future Work

In this paper we present analysis and experimental results that validate the untethered operation of SolarPede a novel light-powered micro-crawler. The microrobot body was fabricated using DRIE technology from SOI wafers with a $cm^2$ footprint. 8 Silicon legs were assembled into compliant socket connectors using a custom micro-assembly station in our lab. The leg layout on the microrobot body ensured that omni-directional 2D motions can be achieved using stick-and-slip of the leg on the substrate. An electronic backpack consisting of a Bluetooth enabled microcontroller, a solar cell, voltage booster, and power electronics was designed and connected to the packaged body of the microrobot. In this configuration, locomotion was studied in the "belly-up" or conveyor configuration by placing a payload similar to the robot mass on top of the inverted legs. Experiments were conducted to verify that by multiplexing power between the actuators, the robot can achieve speeds of 13 µm/second. Further experiments confirmed that the microrobot can be operated from an artificial light concentrator lamp.

In future work, a more compact PCB electronic backpack will be implemented. It will feature two stacked double-sided each with a $15mm^2$ form factor. The top board will contain the BL652 and through hole connection points for the programming of the module after soldering it to the robot. The bottom board will contain the voltage booster and transistor array. The face of the board with the transistors will be glued directly to the SolarPede body. Further testing and analysis of the stick-and-slip gaits during regular "belly-down" operation will be conducted under artificial light sources in our lab. Finally, by combining the SolarPede with a miniature robotic arm such as sAFAM [11], mobile nano-scale manipulation may be accomplished.

## Acknowledgment

This work was supported by NSF Grants #CMMI 1734383 and MRI # 1828355. We wish to thank the Micro Nano Technology Center staff at University of Louisville, for their help with MEMS fabrication.

## References

[1] R. Murthy and D. O. Popa, "Millimeter-scale microrobots for wafer-level factories," in Proceedings of 2010 IEEE International Conference on Robotics and Automation, Anchorage, AK, pp. 488-493, 2010.

[2] A. Hsu, C. Cowan, W. Chu, B. McCoy, A. Wong-Foy, R. Pelrine and C. Velez, "Automated 2D micro-assembly using diamagnetically levitated milli-robots," in Proceedings of 2017 IEEE International Conference on Manipulation, Automation and Robotics at Small Scales (MARSS), pp. 1-6, 2017.

[3] R. Murthy, A.N. Das and D.O. Popa. "Nonholonomic Control for an Assembled Microcrawler," in IFAC Proceedings Volumes 42, no. 16 pp. 627-632, 2009.

[4] R. Murthy, A.N. Das, D.O. Popa and H.E. Stephanou ARRIpede, "An Assembled Die-Scale Microcrawler", in Advanced Robotics, 25:8, pp. 965-990, 2011.

[5] H. Woern, M. Szymanski and J. Seyfried, "The I-SWARM project," In Proceedings of 15th IEEE International Symposium on Robot and Human Interactive Communication, Hatfield, pp. 492-496, 2006.

[6] S. S. Shroff and M. P. de Boer, "Constant Velocity High Force Microactuator for Stick-Slip Testing of Micromachined Interfaces," in Journal of Microelectromechanical Systems, Volume: 24, Issue: 6, pp. 1868–1877, 2015.

[7] J.-M. Breguet and R. Clavel, "Stick and slip actuators: design, control, performances and applications," in Proceedings of International Symposium on Micromechatronics and Human Science. – Creation of New Industry – (Cat. No.98TH8388), pp. 89-95, 1998.

[8] Q. Long, J.S. Park and Y. B. Gianchandani, "Bent-beam electrothermal actuators-Part I: Single beam and cascaded devices," in Journal of Microelectromechanical Systems 10, no. 2, pp. 247-254, 2001.

[9] J.-S. Park, L. L. Chu, A. D. Oliver and Y. B. Gianchandani, "Bent-beam electrothermal actuators-Part II: Linear and rotary microengines," in Journal of Microelectromechanical Systems, vol. 10, no. 2, pp. 255-262, 2001.

[10] K. Tsui, A.A. Geisberger, M. Ellis and G.D. Skidmore, "Micromachined end-effector and techniques for directed MEMS assembly," in Journal of Micromechanics and Microengineering 14, no. 4, pp. 542-549, 2004.

[11] R. Zhang, D. Wei and D. O. Popa "Design, Analysis and Fabrication of sAFAM, a 4 DOF Assembled Microrobot," Proceedings of 2018 IEEE International Conference on Manipulation, Automation and Robotics at Small Scales (MARSS), pp. 1-6, IEEE, 2018.